

# Strain-invariant omnidirectional stretchable MXetronics

Received: 24 July 2025

Accepted: 21 January 2026

Peer Review: 3 January 2026

 Check for updates

Shenglong Wang<sup>1,2,3,5</sup>, Weili Deng<sup>1,5</sup>, Haichao Huang<sup>1,5</sup>, Zhuocheng Yan<sup>4</sup>, Yongbin Wang<sup>1</sup>, Tingting Zhou<sup>1</sup>, Yong Ao<sup>1</sup>, Zihan Wang<sup>1</sup>, Jiabin Zhang<sup>1</sup>, Guo Tian<sup>1</sup>, Boling Lan<sup>1</sup>, Yue Sun<sup>1</sup>, Tianpei Xu<sup>1,3</sup>, Tao Yang<sup>1</sup>, Longchao Huang<sup>1</sup>, Long Jin<sup>1</sup>, Jun Lu<sup>3</sup> & Weiqing Yang<sup>1,2</sup>✉

Titanium carbide MXene flakes hold great promise for system-level MXene-based electronics (MXetronics) due to their outstanding electrical conductivity and diverse functional properties. However, the weak MXene interlayer bonding often causes film fracturing under mechanical strain, ultimately leading to device failure, manifested as unstable operation, inaccurate data transmission, and potential electrical disconnection. Here, we present strain-invariant, omnidirectionally stretchable MXetronics (sos-MXetronics) through hierarchical stiffness microgrid engineering. This strategy synergistically integrates patterned elastiff regions and modulus-buffered interconnects, effectively preventing performance shifts in sos-MXetronics. This circular sos-MXetronics with a radius of 3.3 cm integrates a near-field communication (NFC) antenna, eight micro-supercapacitors (MSCs), three resistive sensors, and interconnected conductive networks, demonstrating exceptional strain invariance with 95–98% performance retention even under 40% strain. With the capability to minimize motion-induced artifacts, the system ensures accurate blood pressure (BP) monitoring without electrical disconnection, even during wrist deformations. This breakthrough not only marks a significant step toward the practical application of MXene in omnidirectional stretchable MXetronics, but also paves the way for reliable, high-performance electronics based on two-dimensional materials for next-generation health-care monitoring systems that seamlessly integrate with the human body under real-world conditions.

Skin-like electronics represent a transformative technology with immense potential for enabling continuous, large-scale, and high-fidelity monitoring of physiological conditions, as well as facilitating real-time health status analysis<sup>1–4</sup>. A comprehensive skin-like monitoring system typically comprises different functional modules, including power supply, sensing, signal acquisition, and transmission units<sup>2</sup>.

However, given that human bodies frequently undergo movements that induce pronounced deformations in the skin, tissues, and organs, the resulting mechanical strain invariably degrades the electrical performance of these functional units, posing a significant challenge to their reliability<sup>5,6</sup>. To address this issue, it is crucial to design skin-like electronics with comparable stretchability. Such electronics must

<sup>1</sup>Key Laboratory of Advanced Technologies of Materials (Ministry of Education), School of Materials Science and Engineering, Southwest Jiaotong University, Chengdu, PR China. <sup>2</sup>Research Institute of Frontier Science, Southwest Jiaotong University, Chengdu, PR China. <sup>3</sup>School of Chemistry, Southwest Jiaotong University, Chengdu, PR China. <sup>4</sup>School of Integrated Circuits, Shandong University, Jinan, PR China. <sup>5</sup>These authors contributed equally: Shenglong Wang, Weili Deng, Haichao Huang. ✉e-mail: [wqyang@swjtu.edu.cn](mailto:wqyang@swjtu.edu.cn)

retain their functionality while conformably attached to surfaces under stretching deformation, ensuring stability in dynamic environments. Considerable efforts have been devoted to developing stretchable and integrable electronics through material innovations<sup>7</sup> and device engineering<sup>8</sup>. Despite these advancements in fabricating individual functional units with enhanced performance under strain, fundamental challenges remain in achieving seamless integration of diverse functional components without compromising reliability under dynamic operating conditions. As electronic systems grow increasingly complex, there is a pressing need to construct all functional components from a single material system, which could simplify integration and reduce manufacturing costs. However, such a strategy is often constrained by the intrinsic limitations of individual materials, which generally fail to satisfy the broad spectrum of performance criteria required by different functional devices (for example, although copper and liquid metals are commonly used in electrical wiring, they are unsuitable for energy storage applications due to inherent trade-offs among electrical conductivity, electrochemical activity, and processability)<sup>6</sup>. Addressing these challenges is essential for advancing the field of skin-like electronics and unlocking their full potential in wearable health monitoring and personalized healthcare applications.

MXene-based electronics, utilizing monolayer  $\text{Ti}_3\text{C}_2\text{T}_x$  MXene flakes with superior mechanical properties<sup>9</sup>, exhibit exceptional intralayer conductivity enabled by the hybridization of transition metal and carbon atoms<sup>10–12</sup>. This unique electronic structure facilitates the efficient spread of electronic states, enabling the development of epidermal soft electronics, “MXetronics”<sup>13</sup>, and provides a versatile foundation for single-material integration. Significant attention has been given to its use in flexible electronics<sup>11</sup>, energy storage<sup>14</sup>, terahertz absorbing<sup>15</sup>, and many others<sup>10,16,17</sup>. An overlooked aspect of this research field is the stretchability of MXene-based electronics. MXene films are fairly stiff and prone to perpendicular fracture under tensile deformations due to weak interlayer interaction<sup>11,14,18</sup>, exhibiting limited intrinsic stretchability (<5%)<sup>10,14</sup>. Such fractures can severely affect in-plane charge carrier transport, compromising electrical performance<sup>19</sup>. This limitation is particularly problematic for sensors and radio frequency (RF) electronics, which are highly sensitive to changes in physical geometries<sup>7,8</sup>. To address these limitations, several strategies such as crack bridging, interlayer insertion, and bio-mimetic architecting have been developed to strengthen interlayer interactions and thereby improve the inherent deformability of MXene-based films<sup>20–22</sup>. Although these methods effectively suppress crack propagation and enable energy dissipation, the introduction of small molecules and polymers inevitably results in considerable conductivity degradation, creating a trade-off between stretchability and electrical performance that remains unresolved. Consequently, these methods are more suitable for strain sensors<sup>23</sup>, where resistance changes with strain, rather than for stretchable electronics that require stable electrical performance under deformation. Introducing various structural designs, such as wrinkled<sup>1</sup>, kirigami<sup>24</sup>, or island-bridge structures<sup>25</sup>, can effectively increase the stiffness and decrease the experienced strain of MXetronics. However, these approaches face limitations in achieving omnidirectional strain tolerance. In practical dynamic environments featuring anisotropic stress distribution and unpredictable multidirectional strains, off-axis stretching beyond designed deformation directions induces severe strain concentration at rigid-elastic interfaces, leading to interconnect failure. To achieve full mechanical stretchability of MXetronics, the adjacent electronics and their interconnections must exhibit strain-insensitive properties.

Here, we report a strain-invariant omnidirectional stretchable MXetronics (sos-MXetronics) that integrates energy storage, wireless communication, and sensing functionalities into a high-consistency material architecture (Fig. 1a, b). The strain-invariant behavior is realized through the synergistic design featuring patterned PDMS elastiff layers on an Ecoflex elastomeric base and stretchable modulus-

buffered polyethylene terephthalate (PET) interconnects, thus enabling localized stiffening and strain redistribution to prevent MXene cracking (Fig. 1c–e). To ensure efficient signal exchange and energy delivery between the sos-MXetronics and the mobile terminal, we developed a high-conductivity (3500 S/cm)  $\text{Li}^+$  exchange MXene, which enables the fabricated system to wirelessly power and sense at distances up to 3.5 cm. Most importantly, the sos-MXetronics exhibits a strain insensitivity with less than 5% performance variation under 40% strain. Finally, the sos-MXetronics demonstrated motion interference-free monitoring of human pulse, temperature, and BP via near-field communication (NFC). The fully demonstrated strain-invariant all-MXene platform offers a powerful tool for large-scale integrated manufacturing of next-generation wearable and stretchable electronics.

## Results

### Design conception and workflow of the sos-MXetronics

The idea of integrated omnidirectional stretchable MXetronics is illustrated in Fig. 1a, where eight micro-supercapacitors (MSCs), three resistive sensors, one NFC antenna, and interconnected conductive networks are ingeniously arranged within a 3.3 cm radius, endowing the entire stretchable system with unparalleled integrity. The circuits, sensors, energy harvesting, and storage components are fabricated on a PET substrate using a spray-coating process and subsequently transferred to a stretchable patterned Ecoflex/PDMS substrate (Supplementary Fig. 1), enabling exceptional flexibility and comfortable attachment to human skin. The MXene antenna achieves an open-circuit potential (OCP) > 3 V, generating over 5 mW average power output to drive the system at maximum power point, which enables fast charging of the MXene MSCs at 50 mA/cm<sup>2</sup>. In series/parallel configuration, the MSCs output 2.4 V with 4.17 mW/cm<sup>2</sup> power density, which is sufficient to sustain the microcontroller unit (MCU) operation. Power sourcing automatically switches between the NFC antenna (near-field mode, ≤3.5 cm) and MSCs (far-field mode) based on proximity. Resistive sensors continuously monitor vital signs (temperature, pulse, and blood pressure), while the MCU digitizes analog signals via an ADC and relays data wirelessly via NFC for cloud analysis. Figure 1b compares the proposed strain-invariant stretchable system with conventional stretchable electronics. Conventional systems exhibit significant performance degradation under strain, including shifted antenna resonance frequencies, drifted sensor calibration values, and reduced energy storage capacity, which collectively lead to measurement inaccuracies and potential wireless signal dropout. In contrast, our sos-MXetronics demonstrates strain-invariant performance, synergistically achieved by patterning PDMS elastiff layers on an Ecoflex elastomer layer with modulus-buffered PET interconnects (Fig. 1c). This design strategically localizes strain to the lower-modulus interspaces between active components, effectively minimizing functional degradation. The serpentine interconnects provide stretchability, while elastiff layers protect the straight-line-based devices to maintain performance stability (Fig. 1d), ultimately forming the stretchable sos-MXetronics. Figure 1e exhibits the unique crack modulation behavior of sos-MXetronics, where applied strain induces localized MXene flake sliding rather than catastrophic through-cracks and large conductive islands, preserving conductive pathways. Comparative analysis (Supplementary Table 1) reveals that the sos-MXetronics system exhibits superior strain-invariant performance (<5% variation under 40% strain), outperforming previously reported integrated electronics based on MXenes and other materials across all key functional metrics (Fig. 1f). The standalone stretchable sos-MXetronics features thin layout (~300 μm thickness) and low-modulus substrate interface, exhibits robust electromechanical performance upon various mechanical deformations (e.g., stretching, bending, and twisting) as verified by both finite element analysis (FEA) and experimental tests (Fig. 1g, h, Supplementary Fig. 2, and Supplementary Note 1).

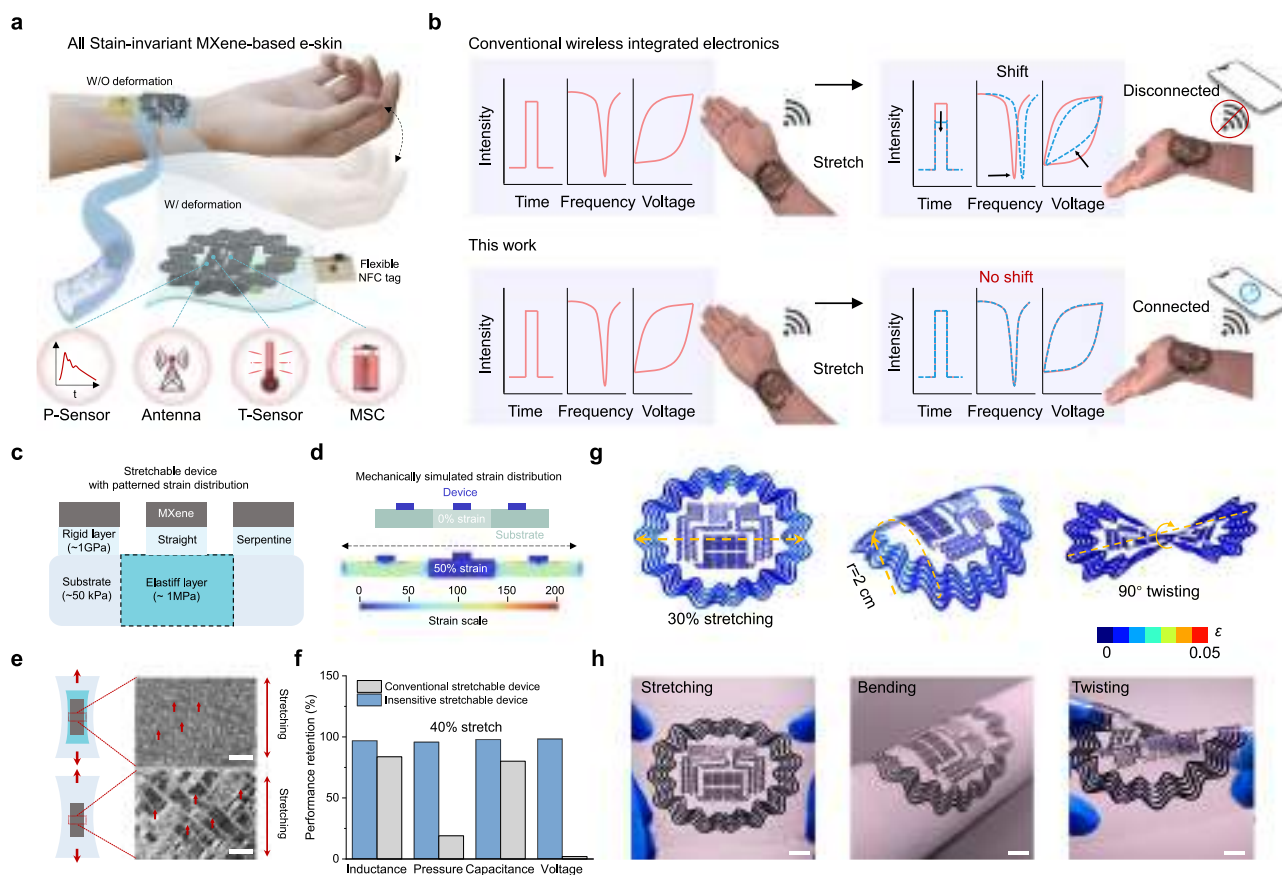


**Fig. 1 | Structure and strain-invariant performance of the stretchable all-MXene microgrid system.** **a** Schematic of the strain-invariant MXene-based wireless system, demonstrating stable operation under deformation or in the non-deformed state. **b** Comparison between the proposed strain-invariant stretchable wireless system and conventional wireless electronics. **c** Two-dimensional diagram showing the representative sos-MXetronics structure. **d** Mechanical simulation showing the strain distribution of a strain-patterned sos-MXetronics for stretching under 50% strain. **e** Optical images showing crack formation and propagation under

stretching. The top image corresponds to the system with a rigid layer and elastif layer, while the bottom image shows the system directly on the substrate. All scale bars are 200  $\mu\text{m}$ . **f** Performance variation of conventional stretchable devices and sos-MXetronics under 40% strain. **g, h** FEA and corresponding experimental results of the sos-MXetronics under mechanical deformations: uniaxial stretching of 30%, bending to the cylinder with a radius of 2 cm, and twisting with a torsional angle of 90°. All scale bars are 1 cm. The experiment was independently repeated three times with similar results.

### Fabrication and characterization of sos-MXetronics

The fabrication of the sos-MXetronics begins with a low-temperature molten salt (LTMS) etching strategy, a rapid and scalable approach that can produce over 100 g of  $\text{Ti}_3\text{C}_2\text{T}_x$  MXene within 5 min (Supplementary Fig. 3 and Supplementary Note 2)<sup>26,27</sup>. This etching duration is two orders of magnitude shorter than the most commonly used etching methods (Supplementary Table 2). The disappearance of the Al (104) peak in the X-ray diffraction (XRD) pattern<sup>28</sup>, along with the accordion-like morphology observed in the scanning electron microscopy (SEM) image and the multilayer structure revealed in the transmission electron microscopy (TEM) image, collectively confirm the successful exfoliation and synthesis of the  $\text{Ti}_3\text{C}_2\text{T}_x$  (Supplementary Fig. 4). To obtain few-layer MXene nanosheets,  $\text{NH}_4\text{HF}_2$ -synthesized  $\text{Ti}_3\text{C}_2\text{T}_x$  is commonly delaminated using large organic molecules such as tetramethylammonium hydroxide (TMAH)<sup>29</sup>. However, the complete removal of  $\text{TMA}^+$  ions is difficult, often resulting in MXene films with larger interlayer spacing, poorer stability, and lower electrical conductivities (<500 S/cm)<sup>30</sup>, which limits their effectiveness in electronic devices. To address this dilemma, we demonstrated an ion-exchange and flocculation method to remove residual organic intercalants (Supplementary Fig. 5, A similar method for  $\text{V}_2\text{CT}_x$  was reported by Yury's group)<sup>31</sup>. Figure 2a illustrates the ion-exchange process, where the surface-adsorbed  $\text{TMA}^+$  ions on MXene are removed and replaced with  $\text{Li}^+$  ions. This process is driven by the electrostatic attraction between the negatively charged 2D MXene and alkali metal cations, as well as the concentration gradient created by

the high concentration of  $\text{Li}^+$  ions (Supplementary Note 3). XRD results show a clear and distinct shift of (002) peak of MXene toward higher Bragg angles (smaller spacing: from 14.6 Å to 12.5 Å) after ion-exchange (Fig. 2b). Thermogravimetric analysis (TGA) also confirmed the removal of residual TMA<sup>+</sup> by the absence of weight loss around 400 °C in the Li-exchanged samples (Supplementary Fig. 6). Note that the Li-exchanged MXene, with an average lateral size of 1.3  $\mu\text{m}$  in its aqueous dispersion, remains stable in its flocculated state for at least two months without degradation. After removing the salt, the flocculated MXene can be redispersed in water (Supplementary Fig. 7). The Li-exchanged films without annealing demonstrate higher conductivity ( $3505 \pm 41$  S/cm) than that of TMA-retained MXene films ( $216 \pm 14$  S/cm) due to the reduced interlayer spacing and the removal of organic molecules, which facilitates electron transport between flakes (Fig. 2c). The conductivity is comparable to that of product obtained by the common conventional HCl/LiF etching method (1000–6000 S/cm)<sup>26,32–38</sup>, while the total synthesized time is reduced to less than one-third of the conventional method (Fig. 2d and “Methods”).

The resulting MXene solution exhibited rheological shear-thinning behavior (Supplementary Fig. 8), enabling continuous extrusion for spraying and quick solidification upon heating to remove most of the intercalation moisture (Fig. 2e). The MXene filaments can be readily sprayed onto various substrates, as evidenced by the identical MXene fingerprints in Raman spectra (Fig. 2f). We used PET as the substrate to support the MXene layers. The PET (modulus of 1.78 GPa,

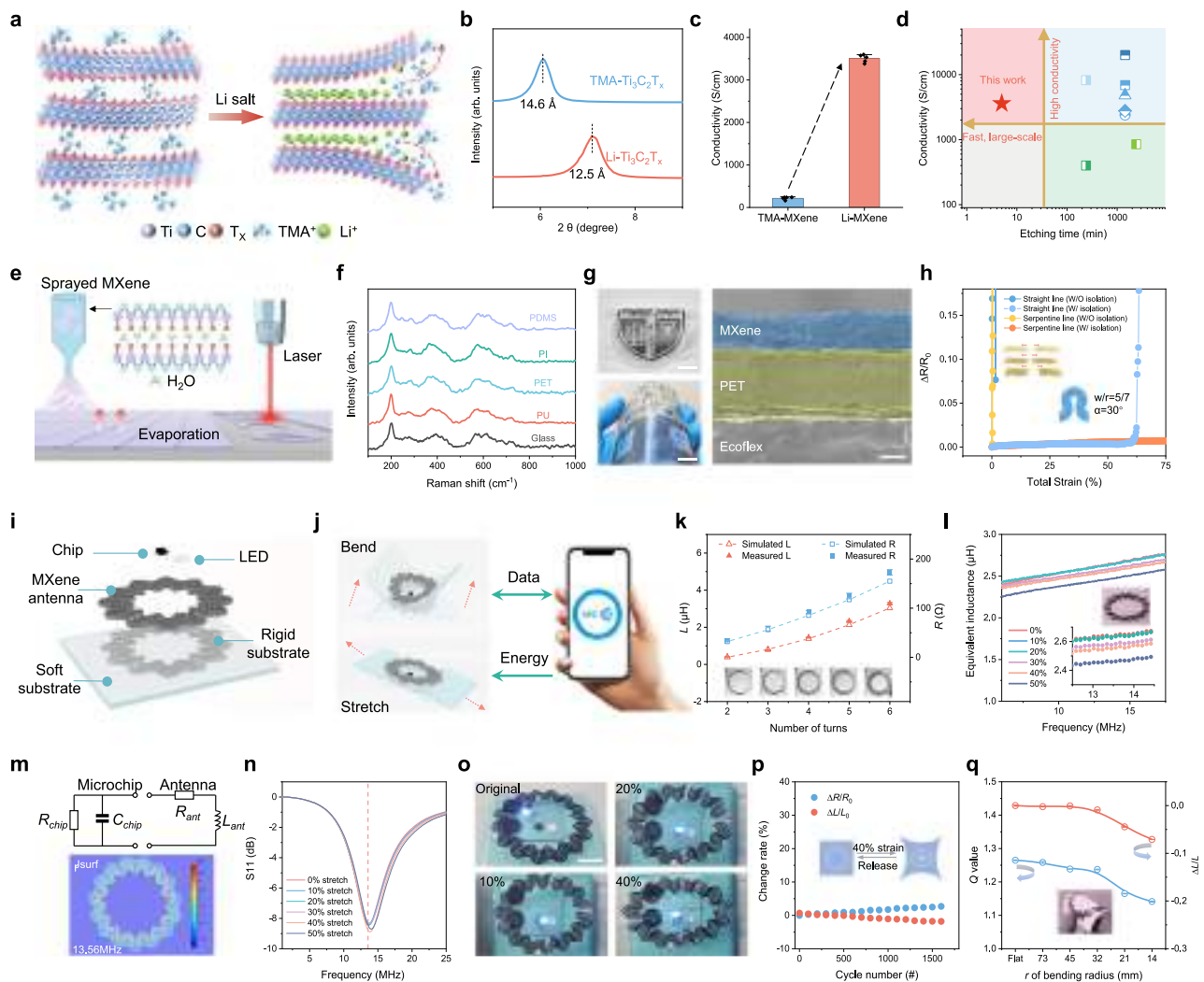


**Fig. 2 | Characterizations of Li-exchanged MXene film and the stretchable MXene antenna.** **a** Schematic of the ion-exchange procedure. **b** XRD patterns of TMA- $\text{Ti}_3\text{C}_2\text{T}_x$  and Li- $\text{Ti}_3\text{C}_2\text{T}_x$ . **c** Conductivity of  $\text{Ti}_3\text{C}_2\text{T}_x$  films with different inter-layer ions (TMA<sup>+</sup>, Li<sup>+</sup>). Data are presented as mean  $\pm$  standard deviation ( $n = 5$  independent experiments). **d** Comparison of the etching time required and conductivity between the other etching methods and our method. **e** Schematic diagram of the spraying and laser cutting process. **f** Raman spectra of patterned MXene on various substrates: polyurethane (PU), polydimethylsiloxane (PDMS), PET, polyimide (PI), and glass. **g** Left: optical image of high-resolution integrated circuits fabricated through direct MXene laser cutting. Scale bars: 2 cm. Right: SEM cross-sectional images of the combined structure of the fabricated integrated circuits. Scale bar: 20  $\mu\text{m}$ . **h**, Relative resistance changes of the four structures under

tensile strain. **i**, Schematic diagram illustrating the fabrication of the MXene NFC system. **j** Diagram illustrating the MXene NFC tag transmitting energy and signals with a smartphone, even under stretching or bending conditions. **k** Simulated and experimentally measured  $L$  and  $R$  values of coils with different numbers of turns (2, 3, 4, 5, and 6). The error bars represent the mean  $\pm$  standard deviation ( $n = 4$  independent experiments). **l** Experimental results of the coil inductance under uniaxial deformation. **m** Equivalent circuit of MXene NFC system and surface current distribution ( $j_{\text{surf}}$ ) of the NFC antenna at 13.56 MHz. **n** Measured  $S_{11}$  parameter. **o** Optical images of MXene NFC tags with the lighted LEDs under uniaxial deformation. Scale bar: 2 cm. **p** Relative changes in  $L$  and  $R$  under cyclic stretching. **q** Changes in  $Q$  and  $L$  under bending.

Supplementary Fig. 9) was selected for its close mechanical match to our MXene films (measured modulus of 6.39 GPa). The PET substrate was plasma-treated and APTES-modified to enable electrostatic assembly of stable MXene layers (Supplementary Fig. 10)<sup>39</sup>. Subsequently, diverse patterned circuits can be efficiently fabricated on various substrates through transferring and programmable laser cutting (Fig. 2g left and Supplementary Fig. 11). We ultimately used Ecoflex with a low modulus (68 kPa) as a stretchable substrate, capable of withstanding up to 660% strain. The Ecoflex-PET adhesion energy was tuned to 87 J/m<sup>2</sup> by UV-ozone treatment, providing sufficient shear resistance while allowing controlled delamination after laser cutting (Supplementary Fig. 12 and Supplementary movie 1). The smooth and continuous cross-sectional interface further confirms the strong bonding and successful layer integration (Fig. 2g). The serpentine

interconnections maintain a relative resistance change below 5% within the functional strain range (up to 75%) in both X and Y directions, while the structure itself can withstand nearly 160% strain before mechanical failure (Fig. 2h, Supplementary Figs. 13 and 14). The rigid serpentine PET island effectively shields the MXene film from large global strain, enabling the electrode to deform through localized MXene flake sliding rather than catastrophic crack propagation. This mechanism prevents the formation of long cut-through cracks and large conductive islands, thereby maintaining electrical integrity even under repeated high tensile strain (Supplementary Figs. 15–18).

**Characterization of MXene NFC system of sos-MXetronics**  
Wireless technologies, particularly RF-based techniques, enable the development of battery-free skin electronics by eliminating the need

for extensive external connections<sup>7,40</sup>. MXene-based NFC antennas are designed to provide emergency power for MXene MSCs and facilitate efficient transmission of sensing signals (Fig. 2i). Notably, geometric deformations can alter the electromagnetic properties of NFC antennas, leading to unstable inductive coupling efficiency. This instability poses a challenge in delivering a consistent power supply for super-capacitors and sensors. To address this issue, we redesign the conventional spiral coil by incorporating a sine-wave modulation, which can ensure uniform stretching of the coil in all directions during elongation (Fig. 2j). To achieve better resonance matching, the geometry of the omnidirectional MXene coils was pre-simulated, showing that the outer radius and the number of turns have the greatest impact on inductance (Supplementary Fig. 19). At a frequency of 13.56 MHz, the inductors displayed similar inductance ( $L$ ) and resistance ( $R$ ) values with the corresponding simulation results (Fig. 2k). To ensure compatibility with the external circuit and space for additional MXene components, the designed sine-wave MXene coil antenna features an inductance of  $-2.7\ \mu\text{H}$ , 5 turns, and dimensions of  $\sim 6.6\ \text{cm}$  in both length and width. Figure 2l shows that the fabricated omnidirectional sine-wave MXene coil exhibits only a 6% change in inductance under extreme elongation of 50%. The stable magnetic coupling area of the coil under 40% strain also reflects this behavior, with a change of only 3.3% (Supplementary Fig. 20 and Supplementary Note 4). In contrast, traditional MXene circular coils, despite good adhesion between PET and Ecoflex, tend to delaminate and suffer nearly 20% inductance variation, leading to electrical disconnection (Supplementary Fig. 21). To match the MXene coils with the NFC chip (NTAG), the resonant frequency of the sine-wave MXene coil can be adjusted by modulating its own capacitance and inductance without an additional matching capacitor to achieve the 13.56 MHz resonance frequency required for NFC operation (Fig. 2m). From Fig. 2n, the as-fabricated MXene NFC antenna exhibits a resonance frequency of 13.57 MHz, with an  $S_{11}$  value of around  $-9\ \text{dB}$ . Although the measured resonance frequency is slightly higher than 13.56 MHz, this hardly affects the energy transmission since more than 70% of the power is transmitted within a 5 dB bandwidth from 11.5 MHz to 16.2 MHz. The MXene antenna can effectively harvest wireless energy from a smartphone to power and light up an LED under stretching conditions (Fig. 2o and Supplementary Movie 2), demonstrating its excellent energy transmission capabilities. The electromagnetic stability of the MXene antenna was validated through over 1500 cycles of 40% uniaxial stretching (Fig. 2p). In addition, the MXene antenna enables bidirectional data exchange under extreme bending conditions (Fig. 2q, Supplementary Fig. 22 and Supplementary Movie 3). The MXene NFC module, with its excellent energy transmission capabilities and data exchange properties under omnidirectional strain, lays a solid foundation for the sensing and energy storage modules in sos-MXetronics.

### Characterization of MXene sensing system of sos-MXetronics

To expand the functionality of our sos-MXetronics, we seamlessly integrated omnidirectional strain-invariant MXene-based pressure and temperature sensors (P-sensor and T-sensor) into the system. This integration achieves additional sensing capabilities without enlarging the device footprint, while the aforementioned MXene antenna ensures a stable power supply. The P-sensor consists of an interdigital MXene electrode and a microstructured PDMS/MXene film (Fig. 3a). Here, a microstructured film with an intermittent architecture was fabricated using large-area programmed laser etching and replica molding, followed by spin-coating MXene nanosheets onto the surface (Supplementary Figs. 23 and 24). Compared with planar and uniform structured films, the intermittent architecture significantly reduces the compressive stress required during deformation (Fig. 3b), with a compressive strength below 50 kPa across the 0–28% strain range. By effectively transmitting pressure from the film surface to the micropillars, this design maintains a low equivalent modulus even under

large strains and facilitates greater changes in contact area (Supplementary Figs. 25 and 26). Extensive experimental data (Fig. 3c) show that the incorporation of intermittent structure also enhances the electrical performance of the sensing film, with the sensitivity of  $56.1\ \text{kPa}^{-1}$  in the low-pressure region, which is about 120 times greater than planar film-based P-sensor (Supplementary Fig. 27). Notably, the effect of interdigitated electrode density and MXene loading on sensor performance is detailed in Supplementary Figs. 28 and 29. Additionally, the sensor demonstrates fast and accurate responses to subtle pressures below 10 kPa (Fig. 3d), and maintains highly stable performance over 25,000 cyclic compressions (Supplementary Fig. 30).

To achieve omnidirectional strain-invariant MXene P-sensors, PDMS was selected as the elastiff layer to enhance the stiffness of the entire P-sensor region. It is worth noting that even the conventional PDMS with 10:1 mixing ratio exhibits a 16-fold higher modulus than that of Ecoflex (Supplementary Fig. 9), minimizing deformation in the active regions of the devices. Moreover, both PDMS and Ecoflex were cured via the hydrosilylation of vinyl and Si-H bonds (Supplementary Fig. 31)<sup>41</sup>, forming a robust adhesive interface capable of enduring large shearing stresses generated by the substantial in-plane strain differences across the interface (Supplementary Fig. 32). The isolated PDMS domains ensure dominant strain accommodation occurs through compliant Ecoflex matrix and serpentine interconnects during stretching, thereby decoupling mechanical deformation from pressure sensing functionality (Fig. 3e). This strain-partitioning mechanism maintains constant interdigitated electrode spacing ( $\Delta D/D_0 < 5\%$ ) across 0–40% strain (Fig. 3f). Without the elastiff layer, the stretching significantly alters the pressure sensing performance over the entire pressure sensing range. For instance, current change readings under the same pressure can vary by up to 80% between no stretching and 40% strain conditions (Supplementary Fig. 33). In contrast, the partially reinforced sensor exhibits negligible performance variation when stretched from 0% to 40% strain (Supplementary Fig. 34). Quantitative analysis reveals a strain insensitivity of approximately 96% (Fig. 3g). Moreover, this strain-invariant pressure sensing performance is well maintained over repeated stretching cycles to 40% strain (Fig. 3h).

In addition to the P-sensor, MXene was also utilized as an active material for wearable temperature sensing. In sos-MXetronics, the MXene-based temperature sensor adopted an omnidirectional strain-invariant serpentine meandering structure (Fig. 3i). By shifting toward the axis of deformation, this design releases stress energy across the pattern, ensuring stable performance during daily use. The MXene T-sensor exhibits a negative temperature coefficient behavior (NTC)<sup>42</sup>, where elevated temperatures enhance charge hopping between MXene flakes, thereby increasing conductivity. The developed MXene T-sensors with different linewidths demonstrated a sensitivity of  $0.95\ ^\circ\text{C}^{-1}$  across a temperature range of  $25\ ^\circ\text{C}$  to  $60\ ^\circ\text{C}$  (Fig. 3j and Supplementary Fig. 35). Under strain (40%), the initial resistance offset was limited to 5%, remaining within an acceptable range (Fig. 3k). Furthermore, the temperature sensor exhibited fast response capability and strain-invariant performance when applied to human skin (Fig. 3l and Supplementary Fig. 36).

### Characterization of wireless harvesting and MXene MSCs charging

To validate the energy harvesting and storage management system, we performed a series of wireless charging and discharging evaluations to assess the robustness and efficiency of the fully MXene-based device. The developed wireless charging system comprises a transmitting unit and a receiving unit, as schematically displayed in Fig. 4a. It operates on the principle of inductive coupling, where the rectifier circuit converts alternating current into direct current to efficiently charge the MXene MSCs featuring interdigitated MXene electrodes and a PVA/ $\text{H}_2\text{SO}_4$  semi-solid electrolyte (Fig. 4b). The interdigitated structure of MSCs plays a crucial role in ion diffusion and transport

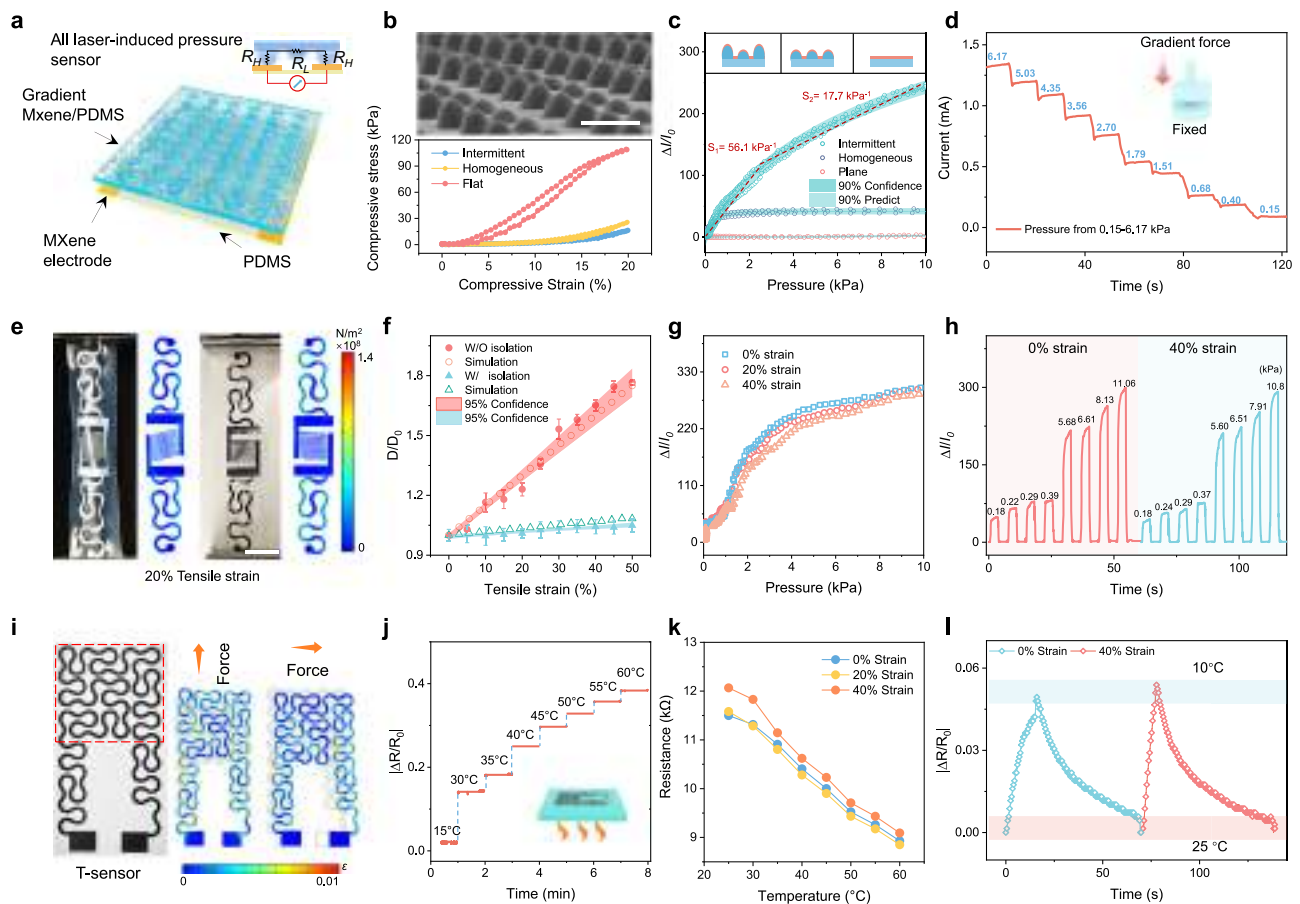


**Fig. 3 | Design and characterization of MXene P-sensor and T-sensor.**

**a** Schematic illustration of the MXene pressure sensor. **b** SEM image of PDMS film with intermittent features and compression tests of flat, uniform, and intermittent PDMS film. Scale bar: 50  $\mu\text{m}$ . The experiment was independently repeated three times with similar results. **c** Relative change in current ( $\Delta I/I_0$ ) of the P-sensors with different microstructures. Solid lines represent the fitted mean response. Shaded regions indicate the 90% confidence interval of the fit and the 90% prediction interval, respectively. **d** Relative changes of the sensor current over time in the gradient static pressure range of 0.15–6.17 kPa. **e** FEA and optical image results of the MXene P-sensor under mechanical deformations. Scale bar: 1 cm. **f** Experimental results of the interdigitated electrode spacing change during

stretching. Error bars indicate  $\pm$  standard deviation from  $n = 4$  independent devices. Shaded areas represent the 95% confidence intervals of the fitted mean trends. **g** Current responses to pressures from the fabricated MXene P-sensor under 0, 20%, and 40% strains. **h** Typical performance of the sensor under pressure loading and stretching cycle between 0 and 40% strains. **i** FEA results and optical image of the MXene T-sensor with mechanical deformations. **j** Dynamic response of an MXene T-sensor under varying temperatures. **k** Resistance responses to temperatures of MXene T-sensor under 0, 20%, and 40% strains. **l** Responses of the temperature sensor under mechanical deformations and periodically changing temperature.

(Supplementary Fig. 37). By optimizing the finger spacing ( $d$ ), width ( $w$ ), aspect ratio ( $l/w$ ), and number of fingers ( $N$ ), the device achieves an areal capacitance of up to 35.4  $\text{mF}/\text{cm}^2$ , with energy and power densities reaching 2.1  $\mu\text{Wh}/\text{cm}^2$  and 4.17  $\text{mW}/\text{cm}^2$ , respectively (Supplementary Figs. 38–42). Additionally, the MXene MSC units can be configured in series or parallel to meet specific power/voltage demands (Supplementary Fig. 43 and Supplementary Note 5). The device also exhibited excellent cycling stability, maintaining 93% capacitance retention after 10,000 cycles (Supplementary Fig. 44). To enhance mechanical deformability, an elastiff layer consistent with the MXene P-sensor region in sos-MXetronics was adopted. Compared with omnidirectional strain-unconstrained MXene MSCs (Supplementary Fig. 45), our device exhibits negligible capacitance change across the 0–40% strain range (Fig. 4c and Supplementary Fig. 46), demonstrating a high capacitance retention rate of 98% (Fig. 4d). Similarly, under bending conditions (Fig. 4e), the capacitance of the MXene MSC increased instead, which can be attributed to the enhanced ion transport properties caused by the contraction of the inner surface during bending (Fig. 4f). When excited by a smartphone, the MXene antenna delivers a stable power output of approximately 5.5 mW (Fig. 4g and Supplementary Fig. 47), which is sufficient to power most

microgrids and systems<sup>5,43,44</sup>. The wireless charging distance can be tuned from 1.9 cm to 3.5 cm depending on the load power (Supplementary Note 6). Furthermore, under 40% strain, the designed MXene antenna maintains an almost constant open-circuit voltage ( $\sim 3.2$  V), showing robust immunity to interference from integrated components while also preventing the strain-induced power interruption typical of traditional circular coils (Fig. 4h and Supplementary Figs. 48 and 49). Following the separate performance characterization of the MXene MSCs and the MXene antenna, the extended energy harvesting and storage function was examined. Based on the self-regulating design principle, the series-parallel MXene MSCs array achieved a voltage window of 3 V, which could be charged to 2 V at a rate of approximately 50  $\text{mA}/\text{cm}^2$  within 2 s (Fig. 4i). The wirelessly charged MXene MSCs array was able to discharge at a constant current of 0.2  $\text{mA}/\text{cm}^2$  for over 460 s. In addition, the charging distance does not affect the charging efficiency (Supplementary Fig. 50). The mechanical stability and transmission efficiency of the synergistic system were evaluated under 0–40% uniaxial stretching and repeated wireless charging-discharging cycles (50 cycles). The capacitance change of the MSCs under these conditions was negligible (Fig. 4j). Further LED illumination tests demonstrated the functions of the

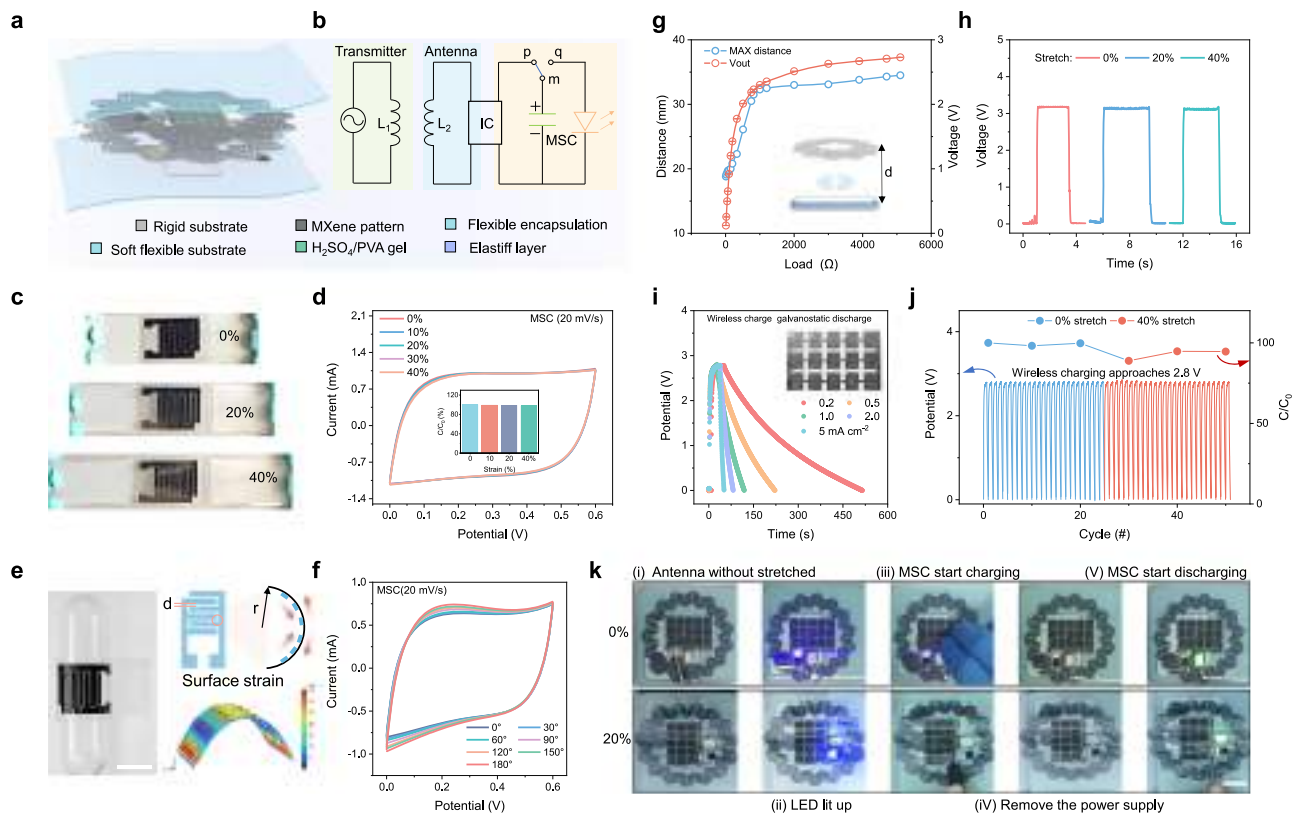


**Fig. 4 | Wireless energy harvesting and charging MXene MSCs.** **a** Schematic illustration of the wireless system integrated with two MXene-based functional modules. **b** Circuit diagram and working mechanism of the wireless charging system. **c** Optical images of MXene MSC under 0%, 20%, and 40% tensile strain. Scale bar: 1 cm. **d**, CV curves acquired from a stretchable MXene MSC under different strains. **e** FEA results and optical image of the MXene MSC under mechanical deformations. Scale bar: 1 cm. **f** CV curves acquired from a MXene MSC under different bending angles. **g** Measured RF-harvested voltage and maximum antenna-

reader distance as a function of load resistance. **h** Open-circuit voltage output of the antenna when stretched at 0%, 20%, and 40% strain. **i** Curves of the wireless charging for the MXene MSCs array with a transmission distance of 2 cm, and galvanostatic discharging at various current densities. **j** Cyclic performance of wireless charging/galvanostatic discharging capability of the integrated system under 0% and 40% strain. **k** Photographs of the MXene-based closed-loop system working under stretching. Scale bar: 2 cm.

MXene-based closed-loop system for energy harvesting, storage, and power supply (Fig. 4k and Supplementary Movie 4).

### Integrated wearable strain-invariant MXene microgrid system

Figure 5a shows a photograph of the fully MXene-based omnidirectional strain-invariant wireless healthcare monitoring system. Detailed fabrication procedures and circuit diagrams are provided in “Methods” and Supplementary Figs. 1 and S1. An ultra-low-power MCU (~400  $\mu$ W), operating below 1.8 V and fully compatible with NFC, enables data acquisition, storage, and wireless transmission to a smartphone (Fig. 5b). The entire sos-MXetronics could withstand 40% tensile strain deformation without any physical damage (Fig. 5c), enabling conformal and biocompatible contact with the wrist for stable, long-term pulse-rate and temperature monitoring (Supplementary Fig. S2). Under full-load operation, the MXene MSC array functions as a backup power source, maintaining system activity for ~10 s after external power removal (Supplementary Movie 5). Furthermore, the pressure and temperature sensors show minimal variation under repeated 40% strain (Fig. 5d and Supplementary Movie 6). Device-level fatigue testing up to 15,000 stretching cycles reveals no detectable degradation in the electrical or sensing performance of the integrated system (Supplementary Fig. S3), confirming its long-term mechanical robustness. In addition, temperature-humidity aging tests demonstrate that the Ecoflex encapsulation effectively suppresses MXene oxidation, enabling stable device operation even after 30 days of environmental exposure (Supplementary Fig. S4). Subsequently, the pulse was measured in a fully wireless and battery-free manner. Natural wrist

movements may induce up to 20% strain at the interface between sos-MXetronics and human skin (Fig. 5e), which often leads to wireless disconnection in traditional MXene-based integrated systems due to changes in RF properties, thereby disrupting accurate sensing data transmission. In contrast, the sos-MXetronics continuously delivers accurate sensing data even under stretching conditions (Fig. 5f). Notably, the elastiff layer-based MXene P-sensor in sos-MXetronics exhibits minimal interference in pulse detection under strain, with the distinct response frequency of the arterial pulse and its higher harmonics validating the stability of our device (Supplementary Fig. S5). Similarly, continuous wavelet transforms (CWT) further confirm that wrist bending has negligible impact on the frequency band (Fig. 5g), with no transient enhancement or attenuation of instantaneous frequencies observed.

Building on these advantages, the sos-MXetronics not only demonstrates precise pulse monitoring capabilities but also holds promise for BP estimation. To ensure reliable coverage of the radial artery, two P-sensors with a working distance of ~2 cm were employed (Fig. 5h), thereby guaranteeing that at least one sensor consistently provides a stable response even in the absence of external preloading pressure (Supplementary Figs. S6 and S7). To effectively capture cardiac cycle characteristics from a single waveform, we identified key points in the segments, as shown in Fig. 5i and Supplementary Table 3<sup>45,46</sup>. Slight variations in waveform morphology among participants were observed due to differences in radial artery depth (Supplementary Fig. S8). Figure 5j shows key features (such as systolic peak time, diastolic peak height and relative augmentation index) extracted

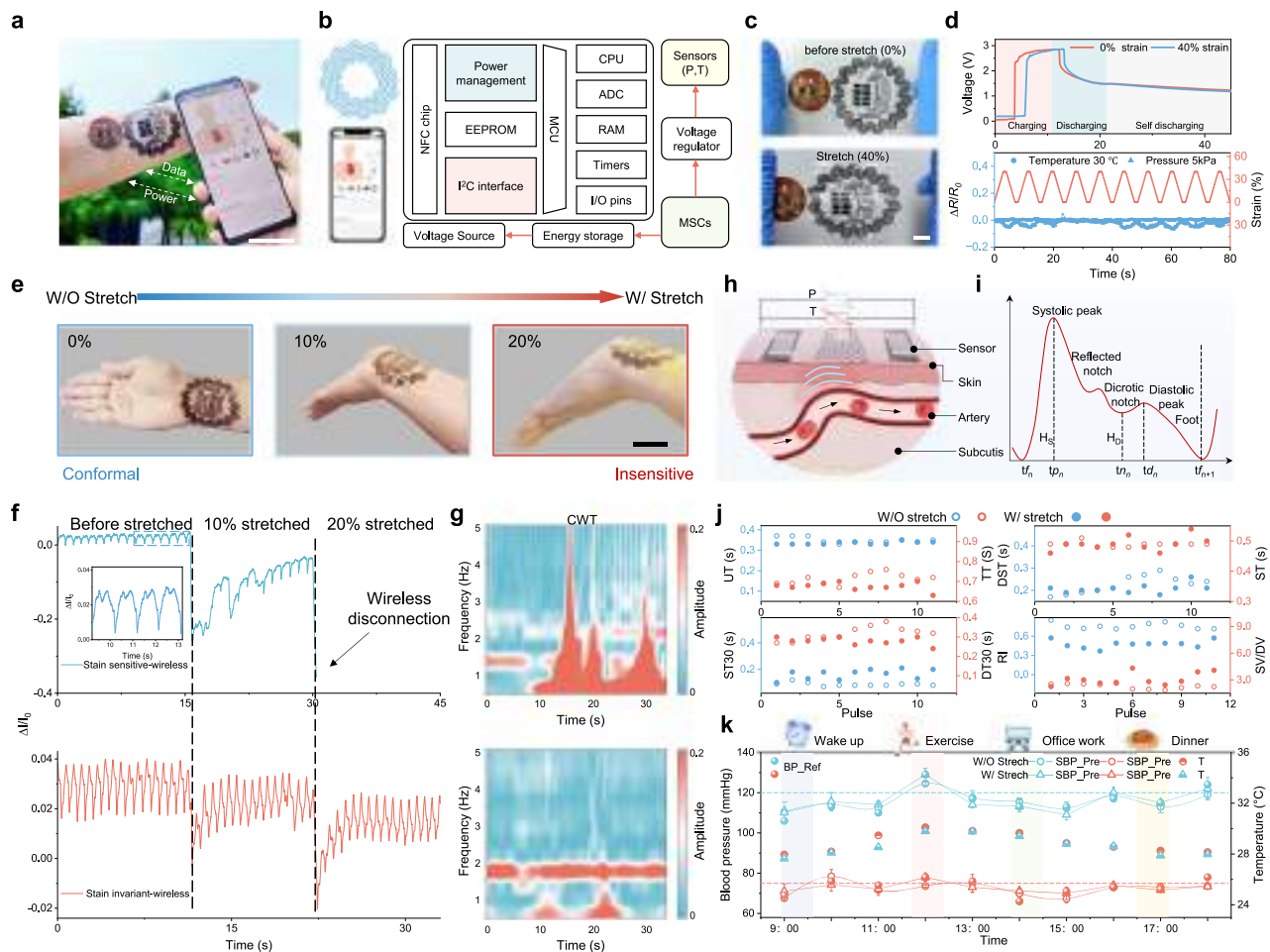


**Fig. 5 | Skin-interfaced wireless microgrid system based on strain-invariant MXene devices.** **a** Optical images of an on-body test of a participant wearing the wireless sos-MXetronics. The collected data were wirelessly sent to a smartphone and displayed in the custom-developed mobile app. Scale bar: 5 cm. **b** Block diagram of the electronic system of the sos-MXetronics. **c** Photographs demonstrating the mechanical compliance of the sos-MXetronics when stretching. Scale bar: 1 cm. **d** Working capacity of each MXene component under strain in sos-MXetronics, as well as its ability to continue functioning without external energy supply. **e** Photograph of the sos-MXetronics on the wrist for the detection of physiological

signals. Scale bar: 2.5 cm. **f** Pulse signals obtained from the sos-MXetronics and strain-sensitive MXene device. The arterial pulse signal is wirelessly disconnected when the antenna is stretched to 20% in strain-sensitive MXene device. **g** Continuous wavelet transforms of pulse signals. **h** Schematic diagram of blood flow and the process of provoking the sensor to generate response. **i** Typical pulse waveform of the radial artery collected by one P-sensor. **j** Feature data extracted from pulse signals collected with and without strain. **k** SBP, DBP, and temperature monitoring throughout the day via sos-MXetronics. The error bars represent the mean  $\pm$  standard deviation ( $n = 4$  independent experiments).

from the pulse waves using our algorithm, inspired by photoplethysmography (PPG)<sup>47</sup>. These features reflect subtle changes in cardiac status. Notably, the minimal fluctuations in these features before and after wrist bending demonstrate the sos-MXetronics's ability to consistently capture high-quality pulse waves even during body movements (Supplementary Fig. 59). Then, the multiple morphological characteristics in the pulse waveform were used as the input for a deep learning training model (Supplementary Fig. 60). The systolic blood pressure (SBP) and diastolic blood pressure (DBP) obtained from a commercial sphygmomanometer (YUYUE) served as reference labels for model training (Supplementary Note 7). The rapid decrease in the loss function during training indicates effective learning and convergence of the model (Supplementary Fig. 61). To further evaluate the agreement between the predicted BP from sos-MXetronics and the measurements from the commercial sphygmomanometer, a Bland-Altman analysis was conducted. These results show mean differences of  $1.51 \pm 6.27$  mmHg for SBP and  $0.87 \pm 4.29$  mmHg for DBP (Supplementary Fig. 62), respectively, reaching the highest Grade A level according to the IEEE standard. In addition, the integrated system maintains stable pulse waveforms and consistent SBP/DBP estimation during walking, jumping, and sweating,

indicating that daily motion and perspiration do not compromise the sensing performance of the sos-MXetronics (Supplementary Figs. 63 and 64). To validate the capability of the sos-MXetronics for long-term and repeated wireless healthcare monitoring, a participant wore the device on the wrist to track physiological parameters including BP and temperature hourly during routine activities such as desk work, meals and exercising (Fig. 5k). The physiological data were translated in real time and displayed on a custom-designed mobile application, with each reading stored in the cloud for access at any time (Supplementary Fig. 65). Clearly, BP showed a significant increase after eating or exercising, while temperature and blood pressure remained stable during wrist bending, demonstrating the device's reliability (Supplementary Movie 7). These results collectively demonstrate the potential of the sos-MXetronics as a completely wireless system capable of delivering clinically relevant data, even under large strain conditions (up to 40% strain).

## Discussion

In this study, we present an omnidirectional strain-invariant, fully MXene-based microgrid system capable of stable operation under both normal and tensile conditions for energy harvesting, storage,

pressure sensing, temperature sensing, and wireless communication. Strain invariance is achieved through the synergistic configuration of patterned elastiff regions and stretchable interconnects securely bonded with the elastomeric substrate, which facilitates effective strain redistribution across the entire device. Comprehensive demonstrations of key stretchable MXene components, such as MXene-based P-sensors, T-sensors, antennas, and MSCs, exhibit exceptional mechanical robustness with less than 5% performance degradation even under 40% strain. As a proof of concept, the sos-MXetronics demonstrates the capability of monitoring human physiological signals across a broad wireless operating range (0–3.5 cm) and strain tolerance (0–40%) without battery. Moreover, the sos-MXetronics significantly minimizes the impact of wrist deformation on the acquisition of pulse and body temperature, greatly enhancing data validity. When integrated with deep learning, the reliably captured pulse signals can further be utilized for continuous blood pressure monitoring throughout the day. The materials, fabrication methods, and design strategies presented here offer new possibilities for achieving multifunctional, closed-loop, strain-insensitive, stretchable electronic devices.

## Methods

### Materials

The MAX precursor was sourced from Jilin 11 Technology ( $\text{Ti}_3\text{AlC}_2$ , 400 mesh). Tetramethylammonium hydroxide (TMAOH, 25%), lithium chloride (LiCl, 98%), polyvinyl alcohol (PVA, 1799 type), and aminopropyltriethoxysilane (APTES, 99%) were purchased from Aladdin Reagent. Ammonium hydrogen fluoride ( $\text{NH}_4\text{HF}_2$ , 98%) was sourced from Shanghai Macklin Biochemical Co. Ltd. Sulfuric acid ( $\text{H}_2\text{SO}_4$ ) and ethanol were obtained from Chengdu Chron Chemicals. Polydimethylsiloxane (PDMS) was purchased from Dow Corning sylgard 184. Ecoflex 00-30 was supplied by Smooth-On, and polyethylene terephthalate (PET) adhesive printing paper was obtained from JiaHan Company. The conductive silver paste was provided by WeiXiuLao Company.

### Synthesis of LTMS- $\text{Ti}_3\text{C}_2\text{T}_x$

(1) Small-batch synthesis of MXene. The LTMS- $\text{Ti}_3\text{C}_2\text{T}_x$  MXene was synthesized by rapidly reacting  $\text{Ti}_3\text{AlC}_2$  and  $\text{NH}_4\text{HF}_2$  molten salt in a two-necked flask. A mixture of 2 g of  $\text{Ti}_3\text{AlC}_2$  and 12 g of  $\text{NH}_4\text{HF}_2$  (98.5%, Shanghai Macklin Biochemical Co., Ltd.) was introduced into the flask within an argon-filled glove box. The flask was then placed in a 130 °C-oil bath, where it was stirred under an argon flow for 5 min. After the reaction, the product was washed multiple times with deionized water to remove impurities. The purified LTMS- $\text{Ti}_3\text{C}_2\text{T}_x$  was dried under vacuum at 40 °C for 24 h. (2) Large-scale synthesis of MXene. For the large-scale production of  $\text{Ti}_3\text{C}_2\text{T}_x$  MXene, 660 g of  $\text{NH}_4\text{HF}_2$  was placed into a 5 L three-neck flask under an argon atmosphere, while 115 g of  $\text{Ti}_3\text{AlC}_2$  powder was introduced into the continuous feeder. The entire system was continuously flushed with argon to maintain an inert atmosphere. The flask was then placed in a 130 °C-oil bath and magnetically stirred. As  $\text{NH}_4\text{HF}_2$  melted,  $\text{Ti}_3\text{AlC}_2$  was steadily fed into the flask from the feeder. After adding  $\text{Ti}_3\text{AlC}_2$  completely, the reaction proceeded for several minutes before removing the flask from the oil bath. The subsequent steps are the same as before.

### Delamination and ion-exchange for Li- $\text{Ti}_3\text{C}_2\text{T}_x$ aqueous inks

Initially, 2 g of  $\text{Ti}_3\text{C}_2\text{T}_x$  was added to 40 mL of 1 M TMAH solution and stirred for 2 h at 50 °C to ensure complete intercalation. After intercalation, the multilayered powder was transferred to a centrifuge tube filled with deionized water (DI water). The solution was centrifuged at  $1200 \times g$  to remove most of the residual TMAH, and the supernatant was discarded. Subsequently, the dispersion was subjected to ultrasound treatment for 1 h under an ice bath and an argon atmosphere. Next, the solution was centrifuged at  $1200 \times g$  for 1 h to obtain a

colloidal dispersion of few-layer TMA- $\text{Ti}_3\text{C}_2\text{T}_x$  nanosheets. To further remove TMAH, a 10 M LiCl solution was prepared and mixed with the TMA- $\text{Ti}_3\text{C}_2\text{T}_x$  dispersion in a 1:5 volume ratio. It is important to carry out this step immediately after preparing the fresh MXene nanosheet dispersion to prevent degradation. After the flocculation of the sample, it was allowed to settle naturally, and after 3 h of ion exchange, the supernatant becomes clear. Subsequently, the flocculated MXene can be washed with deionized water to remove excess lithium ions and redispersed (similar to the washing after intercalation). Specifically, the mixture is centrifuged several times at  $1200 \times g$  to remove the supernatant until the liquid becomes green, and then ultrasonic treatment is applied for 30 min to obtain a uniform Li- $\text{Ti}_3\text{C}_2\text{T}_x$  dispersion.

### Material characterization

The flake sizes of MXene were measured using dynamic light scattering (DLS, Nano ZS). Film morphology and thickness were measured by FESEM (JEOL, JSM-7800F) with an accelerating voltage of 5 kV. The crystalline structure of MAX, LTMS-MXene, TMA-MXene, and Li-MXene was characterized by X-ray diffraction (XRD, Empyrean, PANalytical). The electroconductivity results were obtained using a digital four-probe tester (ST-2258C, JGR). Thermogravimetric analysis was measured using a Mettler Toledo TGA. X-ray photoelectron spectroscopy (XPS) was conducted on Thermo Scientific ESCALAB 250Xi. TEM images of multilayer and few-layer MXene were obtained using a JEM-2100F at an accelerating voltage of 200 kV.

### Fabrication of PVA- $\text{H}_2\text{SO}_4$ gel electrolyte

First, 8 g of  $\text{H}_2\text{SO}_4$  was slowly added to 80 mL of deionized water. After the solution had cooled to room temperature, 8 g of PVA was gradually introduced into the  $\text{H}_2\text{SO}_4$  aqueous solution. The resulting mixture was stirred for 1 h in an 80 °C water bath, allowing it to stand for an additional hour until it returned to room temperature.

### Fabrication of the silicon template and structured MXene/PDMS sensing film

A silicon wafer was patterned using a UV laser marker (UV-3S, Hans Laser). By adjusting the number of laser etching cycles (1–2 times), a template with intermittent structures was created<sup>48,49</sup>. The spacing between the structures was set to 100  $\mu\text{m}$ . The patterned silicon template was treated by chemical vapor deposition of trimethylchlorosilane (TMCS) to enhance mold release properties. A mixture of PDMS base and curing agent (10:1 ratio) was spin-coated onto the silicon template. The coated template was cured at 80 °C for 1 h to produce a PDMS film with microstructures. The PDMS film was carefully peeled from the silicon template and plasma-treated for 5 min to achieve hydrophilicity. The plasma-treated PDMS film was spin-coated with an MXene solution (1 mg/mL). The spin-coating speed was controlled to achieve a tunable MXene coating, producing pressure-sensitive materials.

### Preparation of the sos-MXetronics

(1) Preparation of stretchable substrate. A 200  $\mu\text{m}$  thick Ecoflex film (a mixed liquid of components A and B in a 1:1 ratio, cured at 50 °C for 0.5 h) was used as the stretchable substrate. The Ecoflex film was perforated using a laser cutter (Mingchuang 6090) to create perforated area. PDMS was mixed at a 10:1 ratio and spread to fill the perforated regions of the Ecoflex. The PDMS was then cured at 80 °C for 1 h to form an elastic, hardened region. (2) Surface treatment and coating of PET. The PET film was treated with air plasma (BEK, BMS-150) for 5 min at 100 W. After plasma treatment, the PET was aminated by immersing it in a solution of 10% APTES, 45% ethanol, and 45% water at 50 °C for 30 min. The aminated PET was used as a spray coating substrate. Using a nitrogen gas flow of 0.15 MPa, 100 mL of MXene suspension (10 mg/mL) was evenly sprayed onto the PET substrate

with an area of 20 cm × 15 cm. (3) Attachment of MXene-coated PET to Ecoflex/PDMS substrate. The Ecoflex/PDMS stretchable substrate from step (1) was treated with UV-ozone for 2 min. After that, one side of the PET pattern from step (2) was peeled off and attached to the Ecoflex/PDMS substrate. Air bubbles were removed, and the assembly was left for 1 h to ensure stable bonding. (4) Laser cutting of functional patterns. Using a UV laser marker, the desired patterns, including coils, sensors, supercapacitors, and wires, were cut at a low power setting (20 W). The non-functional regions of the MXene/PET film were carefully peeled off. The MXene coils, MXene temperature sensors, and wires can be used directly. (5) Fabrication of MXene MSCs. A PVA/H<sub>2</sub>SO<sub>4</sub> gel electrolyte was drop-coated onto the interdigital electrode patterns of the supercapacitor portion. The device was allowed to dry at room temperature for 3 h, forming the MXene supercapacitor. (6) Fabrication of MXene pressure sensor. The MXene/PDMS intermittent structured film was laminated onto the interdigital electrode pattern of the sensor portion. The assembly was then sealed with small medical PU tape (50 μm) to ensure stable integration, resulting in the MXene pressure sensor.

### Fabrication of skin-interfaced MXene wireless system

The printed flexible circuit board (FPCB) was designed and manufactured by Jialichuang. Copper wires were then used to establish connections between the MXene devices and the FPCB. Specifically, on the MXene device side, a high-concentration MXene precipitate was first used to establish a connection with the copper wire and the MXene conductor. After curing for 30 min at 60 °C, conductive silver paste was added to reinforce the connection in the bonding area (80 °C for 10 min). Subsequently, an Ecoflex solution with a mass ratio of 1:1 was prepared, then poured and scraped onto the MXene-functionalized areas (such as coils, supercapacitors, etc.) and electrode connections to slow down the oxidation of MXene. The mixture was allowed to cure for 4 h at room temperature.

### Characterization of mechanical properties

PDMS and Ecoflex were cast into dumbbell-shaped molds for tensile testing, while PET was laser-cut into dumbbell-shaped specimens from available rectangular sheets. Serpentine PET and serpentine PET/Ecoflex were directly stretched according to the original pattern. A strain rate of 50 mm min<sup>-1</sup> was applied during stretching, with force and displacement values recorded by the tensile testing machine (LDW-1). For MXene films, these films were laser-cut into rectangular strips (15 mm × 5 mm) for tensile testing under the same conditions. For the peeling test, a silicone rubber adhesive (Sil-poxy, Smooth-On) was used to bond a rigid polyester layer (50 μm thick) to the peeling surface as the backing layer. The sample width varied between 2 and 3 cm, and the peeling speed was kept constant at 50 mm min<sup>-1</sup>. For the compression test, thin films (250 μm) were tested using a precision motor (FET-60).

### Measurements of electromagnetic properties

The electromagnetic properties (S<sub>11</sub>, *Q* factor, impedance, and operating frequency) of the coils within a frequency range of 1–20 MHz were measured by a network analyzer (mini VNA Pro). While testing the coil's resonant characteristic under stretching, a binder clip was used to stretch the coil at different displacements. The changes in electromagnetic properties were recorded by a network analyzer, and a digital camera was used to capture the coil's deformation. The average change in the coil's area was then extracted using ImageJ.

### Characterization of electrical properties of the sensors and electrode

The mechanical data and current changes of the pressure sensor during compression were tested using a mechanical testing system (FET-60) with a computer-controlled platform and a source meter

(Keithley 2450, USA). The temperature sensor was characterized on a hot plate, and the resistance response was recorded using a Keithley-6517B. The resistance of the serpentine MXene/PET/Ecoflex electrode under bending and stretching was measured by the force gauge and source meter mentioned above.

### Cytotoxicity and live/dead assays

Cytocompatibility of Ecoflex and PDMS was evaluated using bone-marrow-derived mesenchymal stem cells (BMSCs). Samples (10 mm diameter) were sterilized and incubated with cells (2 × 10<sup>4</sup> cells per well) in 48-well plates. Cell viability was quantified by a CCK-8 assay (OD<sub>450</sub>, Day 1 and Day 3) and further visualized by live/dead fluorescence staining.

### Electrochemical characterization

Cyclic voltammetry (CV), galvanostatic charge/discharge (GCD), and electrochemical impedance spectroscopy (EIS) were all performed using a CHI660E electrochemical workstation (Chenhua, China). The cycling stability test was conducted using an Arbin MSTAT4 multi-channel potentiostat (Arbin, USA), with a current density of 1 mA cm<sup>-2</sup>. The voltage window for all device tests was 0–0.6 V. EIS testing was carried out at open-circuit voltage, with a frequency range of 100 kHz to 0.1 Hz. The area used in the tests was based on the effective working area of the miniaturized supercapacitors. Detailed calculation formulas for specific capacitance (*C<sub>s</sub>*), energy density (*E*), and power density (*P*) are also provided in Supplementary Note 5.

### Characterization of energy harvesting, storage, and sensing integration

The wireless charging and discharging capability was validated through the source-meter setup. A mobile phone with NFC functionality (Xiaomi 14) was used to power the system. After charging, the system was discharged in GCD mode. After integrating the sensing unit, the MSCs supplied power to the MSP430. The analog signal was then converted into a digital signal by the analog-to-digital converter (ADC) in the MCU. The digital signal was stored in the static random-access memory (SRAM) of the NFC chip. Finally, the data was wirelessly transmitted to a smartphone via the MXene NFC antenna. The data was read and stored using software developed in Android Studio. After the phone was removed, the entire system could be powered continuously by the MXene MSCs.

### Ethical approval

All procedures involving human participants were approved by the Ethics Committee of Southwest Jiaotong University (SWJTU-23012-NSFC(133)). Written informed consent was obtained from all participants. In this study, ten volunteers of different genders (aged 20–30 years) participated in the experiment. The MXene-integrated devices were mounted on their wrists to monitor temperature and pulse. Meanwhile, measurements from a commercial blood pressure monitor (YE600C, Yuyue) were used as a comparative reference. Sufficient blood pressure and pulse data were collected during intense physical activity, and measurements were taken at different intervals. Further processing of the pulse signals and the deep learning model used for blood pressure prediction are detailed in Supplementary Note 7.

### FEA simulation

For the electromagnetic simulation of the coil, a parameterized curve was used to define its shape. The properties of the materials were set as follows: the conductivity of the MXene material was set to 3500 S/cm, and the relative permeability was set to 1. The coil was enclosed in a spherical air domain, with the conductivity of the air sphere set to 0 S/cm. A characteristic impedance of 50 ohms was set at the lumped port. The electromagnetic characteristics of the coil at 13.56 MHz were extracted in the frequency domain. For the mechanical simulation of

the MXene-integrated device, a steady-state solution was used. Specific settings for the simulation can be referenced in Supplementary Note 1.

### Reporting summary

Further information on research design is available in the Nature Portfolio Reporting Summary linked to this article.

### Data availability

The data that support the findings of this study are available from the corresponding authors upon request. Source data are provided with this paper.

### Code availability

No custom code was developed specifically for this study. Data analysis was performed using publicly available third-party code implementing the method described by Su et al.<sup>47</sup>, available at <https://github.com/akrlowicz/ppg-blood-pressure-estimation>.

### References

1. Park, S. et al. Self-powered ultra-flexible electronics via nano-grating-patterned organic photovoltaics. *Nature* **561**, 516–521 (2018).
2. Jiang, Y. et al. A universal interface for plug-and-play assembly of stretchable devices. *Nature* **614**, 456–462 (2023).
3. Song, J. et al. Polyelectrolyte-based wireless and drift-free iontronic sensors for orthodontic sensing. *Sci. Adv.* **11**, eadu6086 (2025).
4. Gong, S. et al. Hierarchically resistive skins as specific and multi-metric on-throat wearable biosensors. *Nat. Nanotechnol.* **18**, 889–897 (2023).
5. Ding, S. et al. A fingertip-wearable microgrid system for autonomous energy management and metabolic monitoring. *Nat. Electron.* **7**, 788–799 (2024).
6. Wang, P. et al. Well-defined in-textile photolithography towards permeable textile electronics. *Nat. Commun.* **15**, 887 (2024).
7. Kim, S. H. et al. Strain-invariant stretchable radio-frequency electronics. *Nature* **629**, 1047–1054 (2024).
8. Su, Q. et al. A stretchable and strain-unperturbed pressure sensor for motion interference-free tactile monitoring on skins. *Sci. Adv.* **7**, eabi4563 (2021).
9. Rong, C. et al. Elastic properties and tensile strength of 2D  $\text{Ti}_3\text{C}_2\text{T}_x$  MXene monolayers. *Nat. Commun.* **15**, 1566 (2024).
10. Wan, S. et al. Scalable ultrastrong MXene films with superior osteogenesis. *Nature* **634**, 1103–1110 (2024).
11. Wu, Y. et al. Orbit symmetry breaking in MXene implements enhanced soft bioelectronic implants. *Sci. Adv.* **10**, eadp8866 (2024).
12. VahidMohammadi, A., Rosen, J. & Gogotsi, Y. The world of two-dimensional carbides and nitrides (MXenes). *Science* **372**, eabf1581 (2021).
13. Kim, H., Wang, Z. & Alshareef, H. N. MXetronics: electronic and photonic applications of MXenes. *Nano Energy* **60**, 179–197 (2019).
14. Yang, J. et al. Water-induced strong isotropic MXene-bridged graphene sheets for electrochemical energy storage. *Science* **383**, 771–777 (2024).
15. Zhao, T. et al. Ultrathin MXene assemblies approach the intrinsic absorption limit in the 0.5–10 THz band. *Nat. Photonics* **17**, 622–628 (2023).
16. Gogotsi, Y. & Huang, Q. MXenes: two-dimensional building blocks for future materials and devices. *ACS Nano* **15**, 5775–5780 (2021).
17. Chu, T. et al. Nanofluidic sensing inspired by the anomalous water dynamics in electrical angstrom-scale channels. *Nat. Commun.* **15**, 7329 (2024).
18. Driscoll, N. et al. MXene-infused bioelectronic interfaces for multi-scale electrophysiology and stimulation. *Sci. Transl. Med.* **13**, eabf8629 (2021).
19. Park, B. et al. Dramatically enhanced mechanosensitivity and signal-to-noise ratio of nanoscale crack-based sensors: effect of crack depth. *Adv. Mater.* **28**, 8130–8137 (2016).
20. Liu, H. et al. Harnessing the wide-range strain sensitivity of bilayered PEDOT:PSS films for wearable health monitoring. *Matter* **4**, 2886–2901 (2021).
21. Feng, B. et al. Nacre-inspired, liquid metal-based ultrasensitive electronic skin by spatially regulated cracking strategy. *Adv. Funct. Mater.* **31**, 2102359 (2021).
22. Liu, Y. et al. Ag-thiolate interactions to enable an ultrasensitive and stretchable MXene strain sensor with high temporospatial resolution. *Nat. Commun.* **15**, 5354 (2024).
23. Gu, J. et al. Extremely robust and multifunctional nanocomposite fibers for strain-unperturbed textile electronics. *Adv. Mater.* **35**, 2209527 (2023).
24. Meng, K. et al. Kirigami-inspired pressure sensors for wearable dynamic cardiovascular monitoring. *Adv. Mater.* **34**, 2202478 (2022).
25. Libanori, R. et al. Stretchable heterogeneous composites with extreme mechanical gradients. *Nat. Commun.* **3**, 1265 (2012).
26. Chen, N. et al. Supercritical etching method for the large-scale manufacturing of MXenes. *Nano Energy* **107**, 108147 (2023).
27. Wang, Y. et al. Ultrafast synthesis of MXenes in minutes via low-temperature molten salt etching. *Adv. Mater.* **36**, 2410736 (2024).
28. Naguib, M. et al. Two-dimensional nanocrystals produced by exfoliation of  $\text{Ti}_3\text{AlC}_2$ . *Adv. Mater.* **23**, 4248–4253 (2011).
29. Naguib, M., Unocic, R. R., Armstrong, B. L. & Nanda, J. Large-scale delamination of multi-layers transition metal carbides and carbonitrides “MXenes”. *Dalton Trans* **44**, 9353–9358 (2015).
30. Alhabeab, M. et al. Guidelines for synthesis and processing of two-dimensional titanium carbide ( $\text{Ti}_3\text{C}_2\text{T}_x$  MXene). *Chem. Mater.* **29**, 7633–7644 (2017).
31. Matthews, K., Zhang, T., Shuck, C. E., VahidMohammadi, A. & Gogotsi, Y. Guidelines for synthesis and processing of chemically stable two-dimensional  $\text{V}_2\text{CT}_x$  MXene. *Chem. Mater.* **34**, 499–509 (2022).
32. Shao, Y. et al. Room-temperature high-precision printing of flexible wireless electronics based on MXene inks. *Nat. Commun.* **13**, 3223 (2022).
33. Ling, Z. et al. Flexible and conductive MXene films and nanocomposites with high capacitance. *Proc. Natl. Acad. Sci. USA*. **111**, 16676–16681 (2014).
34. Shahzad, F. et al. Electromagnetic interference shielding with 2D transition metal carbides (MXenes). *Science* **353**, 1137–1140 (2016).
35. Oh, T. et al. Fast and high-yield anhydrous synthesis of  $\text{Ti}_3\text{C}_2\text{T}_x$  MXene with high electrical conductivity and exceptional mechanical strength. *Small* **18**, 2203767 (2022).
36. Mathis, T. S. et al. Modified MAX phase synthesis for environmentally stable and highly conductive  $\text{Ti}_3\text{C}_2$  MXene. *ACS Nano* **15**, 6420–6429 (2021).
37. Wang, H. et al. Enhancement of the electrical properties of MXene  $\text{Ti}_3\text{C}_2$  nanosheets by post-treatments of alkalization and calcination. *Mater. Lett.* **160**, 537–540 (2015).
38. Zhang, C. et al. Additive-free MXene inks and direct printing of micro-supercapacitors. *Nat. Commun.* **10**, 1795 (2019).
39. Park, T. H. et al. Shape-adaptable 2D titanium carbide (MXene) heater. *ACS Nano* **13**, 6835–6844 (2019).
40. Escobedo, P., Bhattacharjee, M., Nikbakhtnasrabadi, F. & Dahiya, R. Smart bandage with wireless strain and temperature sensors and batteryless NFC tag. *IEEE Internet Things J* **8**, 5093–5100 (2021).

41. Lin, R., Li, Y., Mao, X., Zhou, W. & Liu, R. Hybrid 3D printing all-in-one heterogenous rigidity assemblies for soft electronics. *Adv. Mater. Technol.* **4**, 1900614 (2019).
42. Song, Y. et al. 3D-printed epifluidic electronic skin for machine learning-powered multimodal health surveillance. *Sci. Adv.* **9**, eadi6492 (2023).
43. Gao, C. et al. A seamlessly integrated device of micro-supercapacitor and wireless charging with ultrahigh energy density and capacitance. *Nat. Commun.* **12**, 2647 (2021).
44. Sheng, H. et al. A soft implantable energy supply system that integrates wireless charging and biodegradable Zn-ion hybrid supercapacitors. *Sci. Adv.* **9**, eadh8083 (2023).
45. Li, S. et al. Monitoring blood pressure and cardiac function without positioning via a deep learning-assisted strain sensor array. *Sci. Adv.* **9**, eadh0615 (2023).
46. Li, J. et al. Thin, soft, wearable system for continuous wireless monitoring of artery blood pressure. *Nat. Commun.* **14**, 5009 (2023).
47. Su, P. et al. Long-term blood pressure prediction with deep recurrent neural networks. In: *Proc. IEEE EMBS International Conference on Biomedical & Health Informatics (BHI)* (IEEE, 2018).
48. Wang, S. et al. Mass-produced skin-inspired piezoresistive sensing array with interlocking interface for object recognition. *ACS Nano* **18**, 11183–11192 (2024).
49. Wang, S. et al. Bioinspired MXene-based piezoresistive sensor with two-stage enhancement for motion capture. *Adv. Funct. Mater.* **33**, 2214503 (2023).

## Acknowledgements

The author would like to thank Dr. Qiyun Fan from Tongji University for the support provided in the procedural aspects of this work. The authors acknowledge the Science and Technology Department project of Sichuan Province of China (Grant No. 2024ZYD0013 to W.Y.), the National Natural Science Foundation of China (Grant No. U2330120 to W.D., Grant No.52073237 to J.L.), and the Basic Research Cultivation Project (Grant No. 2682023KJ024 to W.D.). The authors also want to thank the full support from the Analysis and Testing Center of Southwest Jiaotong University.

## Author contributions

S.W., W.D., and H.H. contributed equally to this work. S.W., W.D., and W.Y. conceived and designed the project. S.W., H.H., Z.Y., Y.W., T.Z., Y.A., Z.W., and J.Z. developed the experimental methodology and carried out the device fabrication and measurements. S.W., H.H., B.L., Y.S., T.X., G.T., T.Y., and L.H. performed the systematic investigations, data

collection, and analysis. S.W., Y.W., T.Z., and W.D. conducted data visualization and figure preparation. W.D., L.J., J.L., and W.Y. supervised the research and guided the project execution. S.W., W.D., and H.H. wrote the original draft of the manuscript. All authors analyzed and discussed the results.

## Competing interests

The authors declare no competing interests.

## Additional information

**Supplementary information** The online version contains supplementary material available at <https://doi.org/10.1038/s41467-026-68925-z>.

**Correspondence** and requests for materials should be addressed to Weiqing Yang.

**Peer review information** *Nature Communications* thanks Fuzhen Xuan, and the other, anonymous, reviewer(s) for their contribution to the peer review of this work. A peer review file is available.

**Reprints and permissions information** is available at <http://www.nature.com/reprints>

**Publisher's note** Springer Nature remains neutral with regard to jurisdictional claims in published maps and institutional affiliations.

**Open Access** This article is licensed under a Creative Commons Attribution-NonCommercial-NoDerivatives 4.0 International License, which permits any non-commercial use, sharing, distribution and reproduction in any medium or format, as long as you give appropriate credit to the original author(s) and the source, provide a link to the Creative Commons licence, and indicate if you modified the licensed material. You do not have permission under this licence to share adapted material derived from this article or parts of it. The images or other third party material in this article are included in the article's Creative Commons licence, unless indicated otherwise in a credit line to the material. If material is not included in the article's Creative Commons licence and your intended use is not permitted by statutory regulation or exceeds the permitted use, you will need to obtain permission directly from the copyright holder. To view a copy of this licence, visit <http://creativecommons.org/licenses/by-nc-nd/4.0/>.

© The Author(s) 2026